



AstroSat UVIT Survey of M31: Point-source Catalog

D. A. Leahy , J. Postma, Y. Chen, and M. Buick

Department of Physics & Astronomy, University of Calgary, 2500 University Dr. NW, Calgary, AB T2N 1N4, Canada; leahy@ucalgary.ca

Received 2019 December 11; revised 2020 February 7; accepted 2020 February 11; published 2020 March 16

Abstract

An ultraviolet survey of M31 has been carried out during 2017–19 with the UltraViolet Imaging Telescope (UVIT) instrument on board the *AstroSat* Observatory. Here we analyze far- and near-ultraviolet (FUV and NUV) observations from the M31 UVIT survey, which covers a sky area of $\simeq 3^\circ \times 1^\circ$ with spatial resolution of $\simeq 1''$. The observations included six filter bands in the wavelength range of 120–280 nm. The limiting magnitude (AB) in the FUV band (CaF2 filter), which has the largest number of detected sources, is ~ 23 . The primary product of this work is the M31 UVIT point-source catalog containing positions and photometry. In total $\simeq 75,000$ sources were detected at FUV or NUV wavelengths.

Unified Astronomy Thesaurus concepts: [Ultraviolet astronomy \(1736\)](#); [Ultraviolet sources \(1741\)](#); [Andromeda Galaxy \(39\)](#)

Supporting material: machine-readable tables

1. Introduction

M31 is our closest neighboring large galaxy and is a spiral similar in many ways to the Milky Way. Studies of large numbers of stars have been done in detail for our own Galaxy but have uncertainties related often to uncertain distances or to strong extinction. The advantage of studying objects in M31 is that it is at a well-known distance of 783 kpc (McConnachie et al. 2005).

At optical wavelengths, M31 has been studied thoroughly (e.g., Massey et al. 1986; Davidge 1993; Ibata et al. 2001). Star catalogs have been created for M31, e.g., Massey et al. (2006) presented a catalog of 370,000 stars in M31 in *U*, *B*, *V*, *R*, and *I* bands. *Hubble Space Telescope* (*HST*) carried out a survey of M31 (Bianchi et al. 2012) that included 30 fields imaged in six bands from 170 to 814 nm. This survey covered a small fraction of the area of M31 ($\sim 9 \text{ kpc}^2$ of a total area of M31 of $\sim 300 \text{ kpc}^2$) and produced a catalog of 188,000 sources with *V* and *B* magnitudes (Vega) brighter than ~ 23 . Derived reddening from a spectral energy distribution (SED) analysis ranged from $E(B - V) \simeq 0.1$ up to $\simeq 0.6$. The Panchromatic Hubble Andromeda Treasury (Williams et al. 2014) survey covered a significantly larger area in the central and northeastern parts of M31 ($\sim 1/4$ of the galaxy). It measured six bands from 275 to 1600 nm and cataloged 117 million stars. The above two surveys with *HST* include ultraviolet (UV) bands, where hot, massive stars strongly emit (Bianchi et al. 2014), and so are well suited to studying the massive star populations of M31.

The whole of M31 was observed by *GALEX* (Morrissey et al. 2007) in far-UV (FUV; 154 nm) and near-UV (NUV; 232 nm) bands with spatial resolution of $\sim 5''$. The *GALEX* M31 survey is described in Thilker et al. (2005). A total of 894 star formation (SF) regions with sizes $\geq 1600 \text{ pc}^2$ were detected over the disk of M31 (Kang et al. 2009). *GALEX* and optical data were analyzed by Kang et al. (2012) to derive physical parameters of star clusters and to produce a catalog of 700 star clusters in M31.

A new UV instrument was launched on 2015 September 28 as part of the *AstroSat* mission (Singh et al. 2014). *AstroSat* has four instruments, covering NUV and FUV with the UltraViolet Imaging Telescope (UVIT) telescope and soft through hard

X-rays with the SXT, LAXPC, and CZTI instruments. The UVIT telescope and its calibration are described in Tandon et al. (2017b), Postma et al. (2011), and references therein. The UVIT observations have a high spatial resolution of $\simeq 1''$. Thus, UVIT has the capability of resolving individual stellar clusters and a large number of individual stars in M31.

This paper presents the point-source catalog derived from the *AstroSat* UVIT M31 survey project. The main goal of the survey is to obtain FUV and NUV imaging and photometry for M31 utilizing the high spatial resolution, $\simeq 1''$, of the UVIT instrument. M31 was observed, over a period of ~ 3 yr, with a set of 18 pointings to cover the main body of the galaxy. The survey covers a sky area of about 3° (along the major axis of M31) by 1° (along the minor axis). This is a substantial improvement in coverage over prior works at high ($1''$ or better) resolution in the UV. The primary product of the current work is the M31 UVIT point-source catalog. In Section 2, we describe the observations and data reduction, including astrometry and photometry. We present the M31 UVIT point-source catalog and summarize the catalog in Section 3.

2. Observations and Analysis

The images used in this study were acquired with the UVIT instrument on board the *AstroSat* mission. UVIT is composed of two 38 cm telescopes, one for FUV (130–180 nm) wavelengths and one for NUV (200–300 nm) and visible (VIS) (320–550 nm) wavelengths. The second telescope has a dichroic mirror to split the light into NUV and VIS channels. The field of view for both telescopes is circular with diameter $\simeq 28'$. The FUV, NUV, and VIS channels each have a number of filters with different bandpasses, as described in Tandon et al. (2017b). The VIS channel is operated in integration mode, in order to provide pointing information for the entire set of instruments on *AstroSat*, and is not used for photometry. Science observations are carried out with the FUV and NUV channels, which are operated in photon counting mode.

Further details of UVIT are given in Subramaniam et al. (2016) and Tandon et al. (2017a, 2017b). The pixel size for UVIT images is $\simeq 0''.4168$ by $0''.4168$. Point sources in the UVIT images have FWHM $\simeq 1''.2$ in the FUV and NUV channels. In terms of angular

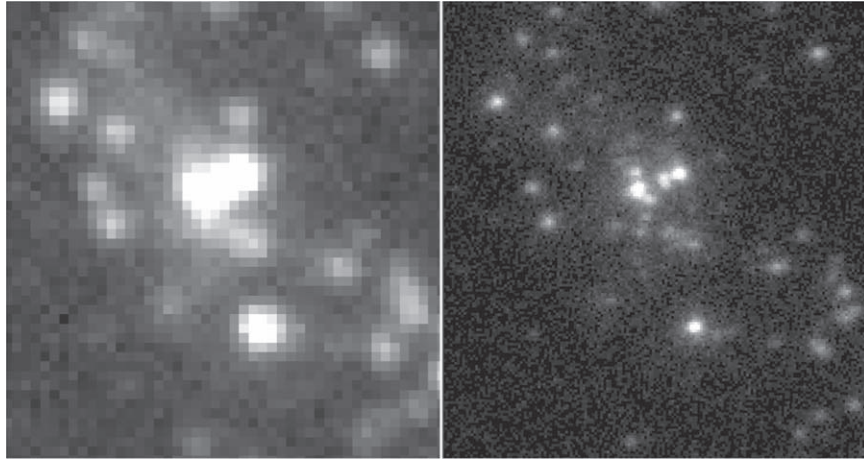


Figure 1. Left panel: full-resolution image from the *GALEX* DIS of M31 for a region $70''$ across in the spiral arm of M31, centered at R.A. 00:44:10.6 decl. +41:33:13 (J2000). Right panel: UVIT FUV CaF2 full-resolution image for the same region.

resolution, the UVIT images are thus a 4–5 times improvement compared to those from *GALEX* ($4''.5$ – $5''.5$). To illustrate the improvement in resolution, Figure 1 compares *GALEX* FUV and UVIT FUV images of the same region, $\simeq 70''$ across, in a spiral arm in M31. The *GALEX* image is from the DIS (Deep Imaging Survey), which is the most sensitive imaging of M31 from *GALEX*. The improvement in resolution is clear and allows photometry of single sources in many more cases than was possible with *GALEX*.

There are sensitivity variations across the detectors of up to $\sim 30\%$, which are fully corrected using calibration data to produce flattened images. The resulting photometric accuracy, within $11'$ of the field center, was found to be 3% for FUV and within 10% for NUV (Tandon et al. 2017b). The astrometric errors for FUV and NUV channels have rms less than $0''.5$ (Tandon et al. 2017b).

For the M31 analysis here we use as much of the outer parts of the $14'$ -radius field of view as possible, in order to maximize the survey area. The emphasis of the Tandon et al. (2017b) study was the inner ($< 11'$ radius) part of the field of view. Thus, we carry our own analysis of photometric and astrometric errors over the whole UVIT field after we carry out source extraction, as discussed in the next section.

For the UVIT M31 survey, 19 fields were observed, but field number 8 did not result in useful data.¹ The sky locations in R.A., decl. (J2000, decimal degrees) of the pointings for the UVIT survey of M31 are shown in Figure 2 overlaid on the DSS Pos2 blue filter image of M31. Table 1 lists the centers for the 18 fields and the different filters used for each field. Exposure times and observation dates (expressed as solar system Barycentric Julian Date) for all field/filter combinations are given in Columns (5) and (6).

The following filters were used for the M31 UVIT survey: CaF2, BaF2, Sapphire, and Silica (for the FUV channel) and NUV B15 and NUV N2 (for the NUV channel). The initial part of the survey was carried out in four filters, FUV CaF2, FUV Silica, NUV B15, and NUV N2. Because of the failure of the NUV channel on the instrument partway through the survey, and because of lower sensitivity than anticipated in the FUV Silica filter, the remaining part of the survey was carried out

with FUV CaF2 and FUV Sapphire filters.² Thus, the whole area of M31 was covered by the FUV CaF2 filter, and parts of M31 were covered in each of the other filters.

Images were corrected for geometric distortion, flat-field illumination, and spacecraft drift using the UVIT-customized software package CCDLAB (Postma & Leahy 2017). A target observation consists of many separate, ~ 400 – 800 s individual observations, one per satellite orbit, each with its own pointing, field rotation, and pointing-drift oscillation. Typical pointings differ by $\sim 5'$. The orbit images are individually drift-corrected and then shifted and rotated for the sum into a final image. For objects near the center of the field, the object never drifts outside the field of view in any of the pointings. For objects near the edge of the field, the object is outside the field of view for parts of the observation. The first time this concern has arisen for UVIT is for the M31 images. Previously, data near the field edges were discarded, and exposure was calculated assuming that objects remain in the field of view for the entire observation, i.e., the exposure map was uniform. We are in the process of upgrading the CCDLAB UVIT pipeline software to produce exposure maps for the entire field of view, including the parts that are observed for only part of the total observation.

The drift-corrected per-orbit images of a single observation are registered to each other using point sources in the per-orbit images, to create a registered image. The world coordinate solution for the registered image is created by a new automated algorithm (J. Postma & D. Leahy 2020, in preparation) implemented in CCDLAB. This matches approximately 100 sources per image found by a new point-source extraction algorithm in CCDLAB (J. Postma & D. Leahy 2020, in preparation) to catalog entries in the BPMag from the *Gaia* Data Release 2. The world coordinate solution follows the CD-Matrix standard for the Gnomonic projection as discussed in Calabretta & Greisen (2002).

2.1. M31 FUV Mosaic

All 18 fields were observed in the FUV CaF2 filter; thus, we construct a full mosaic FUV image of M31 (i.e., full coverage except for the part covered only by F8). All science analysis is done on the unbinned images of the individual fields F1–F19. The purpose of the mosaic image is to display as much as

¹ Field number 8 was observed, but the data were not useful because the *AstroSat* pointing for that observation was not controlled well enough to reconstruct any images.

² One field was observed with FUV CaF2 and FUV BaF2 filters.

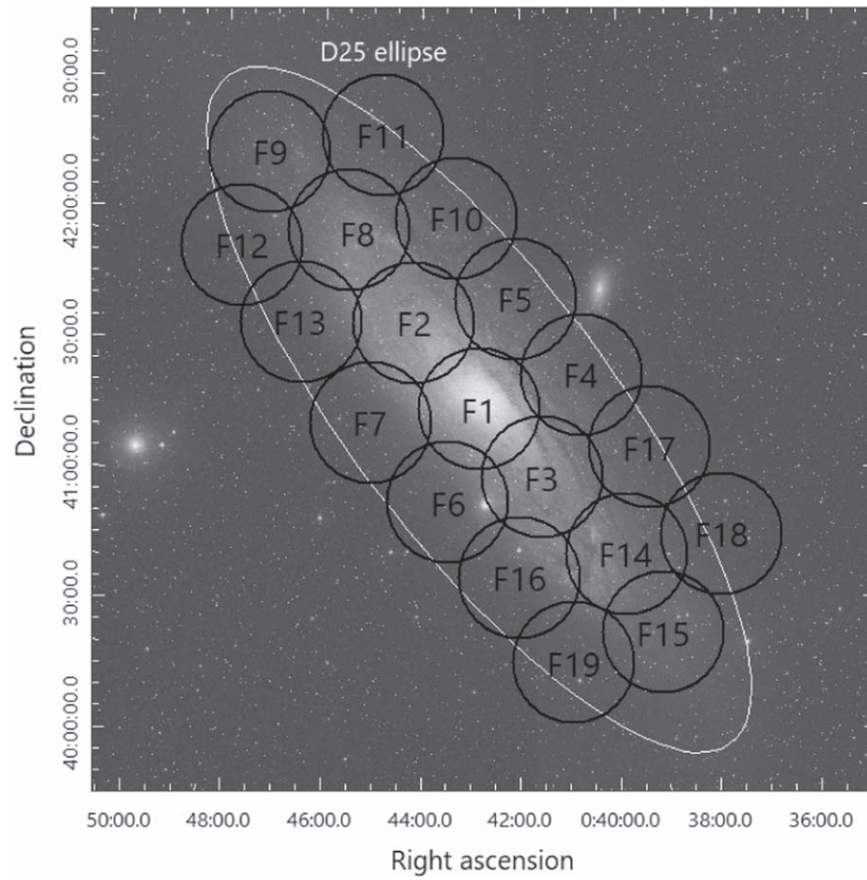


Figure 2. Sky locations in R.A., decl. (J2000, decimal degrees) of the fields/pointings for the UVIT survey of M31, showing the field of view for the fields, labeled F1 to F19 in black. The background image is the DSS Pos2 blue filter image of M31. The white ellipse shows the size of the D25 ellipse for M31, from Gil de Paz et al. (2007). The F8 observations did not produce any useful data.

Table 1
M31 UVIT Observations

Field	R.A.(deg) ^a	Decl.(deg) ^a	Filter ^b	Exposure Time ^c	BJD0 ^{c,d}
1	10.71071	41.25023	a, e, f	7736, 7774, 3624	2,457,672(+0.1273, +0.1272, +0.2626)
2	11.03700	41.55735	a, d, e, f	7927, 1923, 7984, 2156	2,457,704(+0.2031, +0.5581, +0.2031, +0.5579)
3	10.34596	40.95242	a, d, e, f	4998, 9240, 10892, 5045	2,458,066(+0.5196, +0.8437, +0.7897, +0.4470)
4	10.17567	41.32013	a, d, e, f	4955, 10093, 8957, 4975	2,458,067(+0.3167, +0.5345, +0.4618, +0.2486)
5	10.49771	41.62544	a, d, e, f	4954, 10056, 10403, 5024	2,458,068(+0.6680, +0.9387, +0.9386, +0.6680)
6	10.85308	40.85233	a, d, e, f	4998, 9150, 9169, 4494	2,458,070(+0.3654, +0.7083, +0.7082, +0.5831)
7	11.22142	41.16111	a, d, e, f	4964, 10597, 10781, 3135	2,458,071(+0.1874, +0.3901, +0.3900, +0.1874)
8	n/a	n/a	n/a	n/a	n/a
9	11.71750	42.20344	a, b	7260, 7573	2,458,356(+0.8510, +1.1315)
10	10.83346	41.93324	a, d, e	4974, 10184, 15331	2,458,091(+0.2001, +0.4815, +0.1486)
11	11.18496	42.25849	a, d, e, f	4953, 10697, 10805, 5001	2,458,072(+0.0599, +0.2579, +0.2579, +0.0598)
12	11.92225	41.85848	a, d	4161, 8841	2,458,334(+0.2520, +0.5907)
13	11.59533	41.53595	a, d, e, f	4974, 10127, 10188, 5009	2,458,092(+0.2834, +0.7571, +0.7570, +0.2833)
14	9.993958	40.62872	a, c	4720, 10421	2,458,426(+0.8876, +1.0418)
15	9.801542	40.28837	a, c	4724, 10443	2,458,435(+0.1423, +0.2777)
16	10.51008	40.55778	a, c	4796, 10233	2,458,428(+0.3809, +0.7862)
17	9.808417	40.9869	a, c	4730, 9996	2,458,426(+0.0091, +0.1606)
18	9.476917	40.68349	a, c	4747, 8856	2,458,448(+0.2680, +0.4884)
19	10.19363	40.25021	a, c	4768, 10425	2,458,427(+0.5827, +0.9153)

Notes.

^a R.A. and decl. are the J2000 coordinates of the nominal pointing center of the observation.

^b Filter labels are (a) FUV CaF2, (b) FUV BaF2, (c) FUV Sapphire, (d) FUV Silica, (e) NUV B15, and (f) NUV N2.

^c The multiple entries correspond to the respective filters listed in the Filter column.

^d BJD0 is the solar system Barycentric Julian Date of the start of the observation. The common integer part for multiple-filter observations is given as the first number, and the numbers in brackets are the fractional parts.

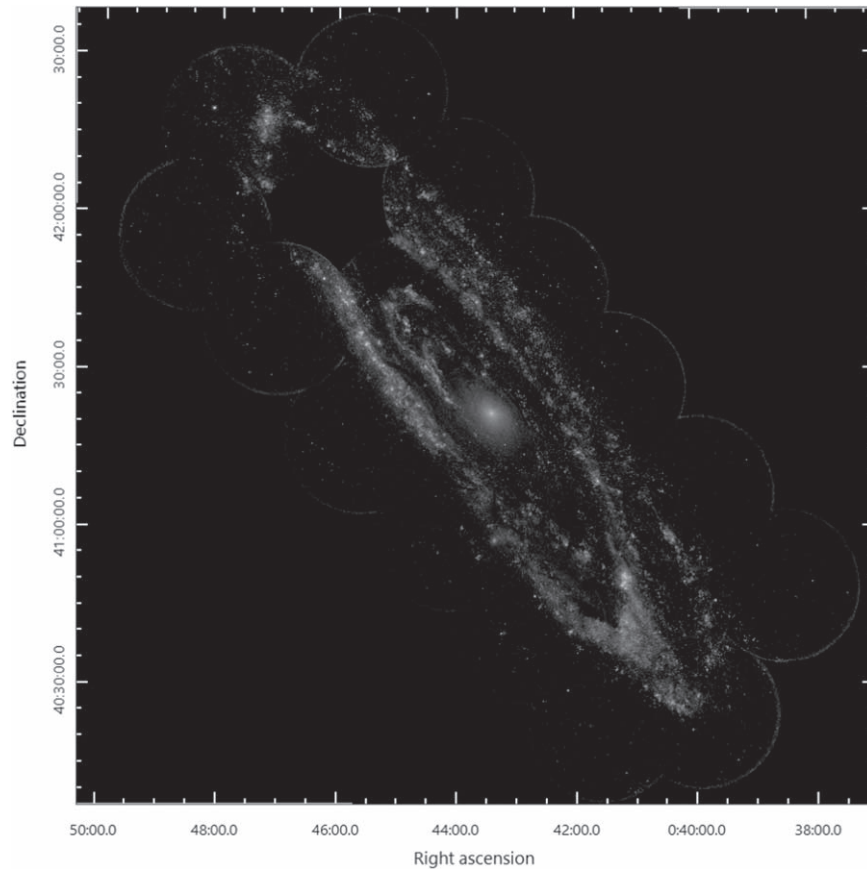


Figure 3. UVIT FUV CaF2 mosaic of M31, $\sim 2.5^\circ$ wide by 2.5° high, centered at R.A. $10^\circ 6848$, decl. $41^\circ 2691$ (J2000). This includes 18 UVIT survey fields.

possible of the full survey observations. The 4800 by 4800 images for each field were binned using the `ftools` task `fimgbin`, to reduce their sizes to 1200 by 1200.

To create a count-rate mosaic image, we summed the individual 1200 by 1200 counts images from all fields to create a counts mosaic, and we summed the individual exposure maps for all fields to create an exposure mosaic. Then, we divide the counts mosaic by the exposure mosaic. Because a uniform exposure across the image for each image was assumed, but the true exposure at the edges of the field can drop to very low values, this procedure yields too high an exposure around the edge of the field and results in dim areas in the mosaic image around the field edges. We tested different corrections to this and found a method that approximately corrects for this. In this method, we use full exposure for pixels with nonzero counts and use zero exposure for the pixels with zero counts to create corrected exposure maps. As noted previously, we are developing an accurate exposure calculation as part of the redesign of the UVIT data reduction software.

The Ximage software was used to create the counts mosaic from the field images and the exposure mosaic from the corrected exposure maps. The counts mosaic was divided by the corrected exposure time mosaic to produce the final FUV CaF2 mosaic of M31, shown in Figure 3. Higher noise levels at the edges of the 18 fields are visible in cases where the edge of the field does not overlap any exposure from another field. Where the edges of one field overlap another field, the combined counts and combined exposure are large enough that the noise is low. For example, northwest of the bulge, the

overlap of fields F4 and F5 shows little noise, but the northwest edges of F4 and F5 show high noise. All subsequent analysis for the UVIT catalog of M31 was done using the individual field images at full 4800 by 4800 resolution.

2.2. Astrometry

The UVIT fields were position calibrated in two steps. For the first step, if the long-wavelength (280 nm) UVIT NUV N2 image existed for a given field, sources in the NUV N2 image were matched to *Gaia* positions. The resulting vector offsets were used to calculate a best-fit field rotation and scaling, which minimized the position offsets. The rotation and offset were applied to create J2000 coordinates for the UVIT NUV N2 image. If the NUV N2 image did not exist, the NUV B15 image or CaF2 image was chosen for coordinate calibration.

Table 2 lists the 18 UVIT fields, the filter for each field that was calibrated with *Gaia*, the number of *Gaia* position calibrators, and the standard deviation of offsets after position calibration. The position errors ranged from a low of $0''.15$ for fields 3 and 7 to a high of $0''.7$ for field 19. The only other fields (than 19) with position offsets from *Gaia* larger than $0''.4$ were field 12 ($0''.43$), 16 ($0''.47$), and 17 ($0''.53$). The larger position errors are not correlated with number of position calibrators and instead are likely caused by residual detector distortion effects and drift correction errors.

Figure 4 shows a test of the position calibration for Field 3. A set of the brightest 86 UVIT sources were used for the position calibration. Then, a larger and fainter set of 690 UVIT sources were matched to *Gaia* to test the position calibration.

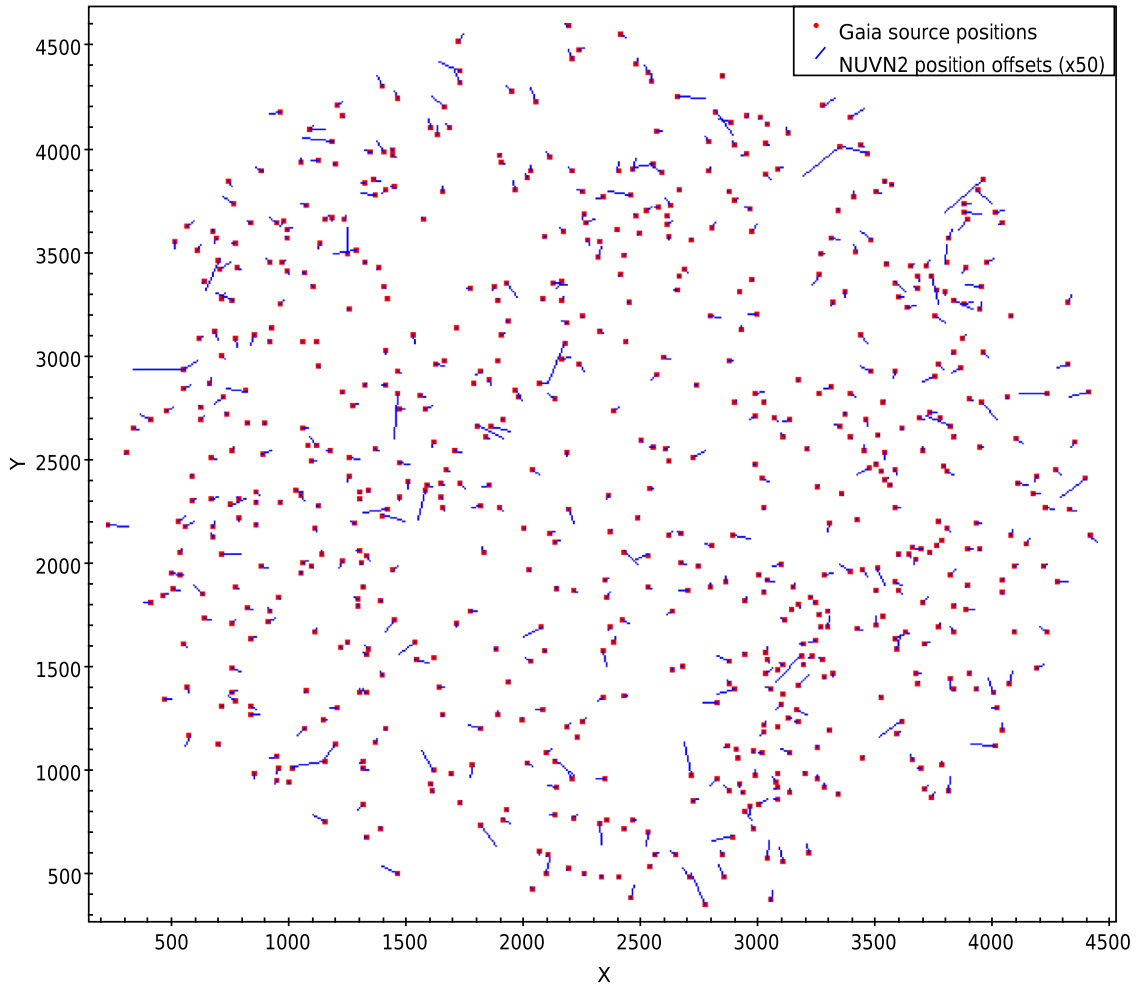


Figure 4. Position offsets of 690 UVIT NUV N2 sources from matched *Gaia* sources for Field 3 in image coordinates, X , Y . The size of 1 pixel is $0''.4168$. The mean offset of UVIT NUV N2 positions from *Gaia* positions is $0''.265$, the largest offset is $1''.87$, and the standard deviation of offsets is $0''.265$.

Table 2
UVIT Fields Astronomy Errors

Field	StDev ^a	No. Calibrators	Field	StDev	No. Calibrators	Field	StDev	No. Calibrators
1 ^b	0.189	154	2 ^b	0.212	108	3 ^b	0.152	86
4 ^b	0.196	93	5 ^b	0.226	101	6 ^b	0.22	118
7 ^b	0.152	17	8	n/a	n/a	9 ^c	0.289	185
10 ^d	0.392	222	11 ^b	0.283	147	12 ^c	0.428	59
13 ^b	0.24	122	14 ^c	0.311	125	15 ^c	0.239	182
16 ^c	0.472	240	17 ^c	0.531	166	18 ^c	0.315	40
19 ^c	0.696	131						

Notes.

^a StDev is the standard deviation of positions with respect to *Gaia* positions in units of arcseconds.

^b NUV N2 is the filter image used for calibration with *Gaia* positions.

^c FUV CaF2 is the filter image used for calibration with *Gaia* positions.

^d NUV B15 is the filter image used for calibration with *Gaia* positions.

The *Gaia* positions and the vector offsets of the NUV N2 positions for the 690 sources are shown. If there were no residual image distortions, after correction in the UVIT pipeline, one would expect the applied rotation and offset from fitting the original 86 NUV N2 sources to the *Gaia* catalog to give an exact match of positions across the field. Also one would expect the standard deviations listed in Table 2 to be zero. However, there are residual distortions. These can

be estimated when we compare the *Gaia* positions to the larger set of UVIT NUV N2 positions. For Field 3, we see that the standard deviation is $0''.265$, somewhat larger than the $0''.15$ from the original set of 86 position calibrators. Figure 4 shows that most of the offsets are small, but that $\sim 10\%$ of the sources have significantly larger offsets. A few of these may be caused by incorrect cross-matching, i.e., a source emitting in the *Gaia* wave bands may be a different source than the one detected in

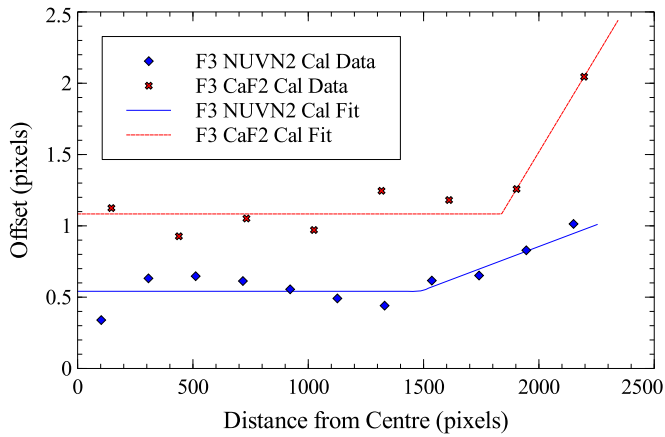


Figure 5. Binned UVIT-*Gaia* position offsets vs. distance from field center for Field 3. The size of 1 pixel is $0''.4168$. The standard position calibration using the NUV N2 image is labeled as F3 NUV N2 Cal. An alternate position calibration using UVIT sources from the FUV CaF2 image is labeled as F3 CaF2 Cal. The best-fit piecewise lines for the two cases are shown. The mean position error for NUV N2 fields calibrated with *Gaia* positions is $\sim 0''.25$ (inside ~ 1600 pixels from the field center), whereas fields calibrated using FUV CaF2 have a mean position error of $\sim 0''.5$.

NUV N2, because of different SEDs. But most are likely caused by distortions in the image that are not corrected by the UVIT pipeline.

A majority of the sources with large offsets occur in the outer parts of the field, where the image distortion is expected to be larger, and where the corrections are expected to be more uncertain. Figure 5 shows the binned UVIT NUV N2-*Gaia* offsets versus distance from the field center for Field 3. It is seen that the mean offsets increase for the outer parts of the field. Inside a radius of $600''$ ($10'$), the mean offset is fairly constant at $0''.2$, and it rises to $\sim 0''.4$ near the outer edge.

We carried out a separate test by calibrating the UVIT CaF2 image to *Gaia* instead of the NUV N2 image. Because there are fewer sources in common between the FUV CaF2 sources and the *Gaia* sources, we expect somewhat larger calibration errors. The resulting mean offsets versus radius are shown in Figure 5. The calibration using the CaF2 image results in the mean offset for the central part of the field of $\sim 0''.4$, which rises to $\sim 0''.8$ for the outer part of the field. This confirms the decision to use the NUV N2 image wherever possible for position calibration.

The second step of the position calibration was to register all of the UVIT images using bright sources common between the different FUV and NUV filters. Since there were many (hundreds) sources and the crowding of bright UVIT sources was not significant, the registration of the images in different filters presented no problems. The J2000 coordinates were then transferred from the calibrated UVIT filter image to the other UVIT filter images. For 9 of the 18 fields the NUV N2 filter image was used for calibration with *Gaia* and the NUV N2 calibration transferred to the other filter images. For one field the NUV B15 image was used, and for eight fields the CaF2 image was used (see Table 2).

2.3. Source Photometry

The source-finding algorithm in CCDLAB was used to carry out basic data analysis tasks and extract point sources for each of the 52 images for the 18 fields of M31 (see Table 1). Isolated point sources in the UVIT images were fit with elliptical

Gaussian and elliptical Moffat functions (Postma & Leahy 2017) to measure point-spread function (PSF) and its variation across each field, as well as its variation between different filters. A Moffat function better fits the PSF profile than a circular or elliptical Gaussian function. Because elliptical Gaussian in all cases gives better results than circular Gaussian, we use elliptical Gaussian in the comparisons discussed below. We found the spatial resolution was $\sim 1''.1$ (FWHM) for FUV and NUV filters.

We compared elliptical Gaussian fits and Moffat fits to curve-of-growth (COG) analysis, as well as with radial profiles for ~ 10 isolated point sources per image (each different field and different filter). The radial profiles exhibit the known extended low surface brightness wings of UVIT's PSF (Tandon et al. 2017b). Because of the extended wings of the PSF, the COG analysis gives the most accurate measurement of total counts from a source. Both Moffat and elliptical Gaussian fits systematically underestimate the total counts per source. We measured the ratio of total counts from COG to that from Moffat fits for ~ 100 isolated bright point sources and found a mean ratio of 1.184 with standard deviation (stdev) of 0.055. In comparison, the ratio of counts from COG to that from elliptical Gaussian fits had a mean of 1.818 and stdev of 0.031. That is, the ratio is constant to within $\sim 5\%$ for Moffat fits and to within $\sim 5\%$ for Gaussian fits. The correction factor between flux from Moffat fits or from elliptical Gaussian fits and flux from COG analysis was compared for different fields and filters and found to be independent of field and filter.

The UVIT M31 images have areas with isolated sources, but a significant fraction of the sources occur in crowded regions. Thus, we found that COG analysis was not possible for a large number of sources. We also found that the Moffat fits failed to converge in crowded regions because they require an extended area without nearby sources contaminating the background area. Elliptical Gaussian fits were found to be reliable even in crowded regions, provided that we took the following precautions: nearby sources were at least $\sim 3''$ away and we restrict the fitting box to be small enough ($\lesssim 3''$) so as not to include nearby sources; we restrict the FWHM along major and minor axes to be consistent with the FWHM values of the PSF derived from fitting bright isolated point sources. The reason is that the elliptical Gaussian function is a good representation of the core of the PSF without any unnecessary parameters that can be confused by the PSF wings of nearby sources. By carrying out tests for different fields and for different filters, we found that restricting the FWHMs to be in the range of $1''.1$ – $1''.3$ for fitting individual sources gave the best results. This is likely because the detector resolution varies slightly from source to source and the slight noncircularity of the beam varies slightly from source to source, possibly related to pointing-drift corrections. Local background for each source was a free parameter in the fits.

2.4. Source Extraction

Photon counting noise is large for sources with a low number of detected counts, such as around the field edges where the exposure time is low or for faint sources. Basic source extraction with a low signal-to-noise ratio (S/N) threshold resulted in many false faint source detections. These were clearly visible as a ring of sources around the edge (outer $\sim 4'$) of each circular field. Convolving the image with a Gaussian smoothing function prior to source extraction gave greatly improved results. Tests showed that using a Gaussian with

Table 3
M31 Source Extraction Regions

Field	Filter	ROI X–Y Center	ROI X–Y HW ^a	Filter	ROI X–Y Center	ROI X–Y HW ^a
1	FUV CaF2	2395, 2395	1980, 1985	NUV B15	2480, 2535	1985, 1980
	NUV N2	2460, 2550	1960, 1985			
2	FUV CaF2	2460, 2225	1985, 2015	FUV Silica	2450, 2210	1950, 2015
	NUV B15	2400, 2375	1965, 1990	NUV N2	2355, 2415	1905, 1965
3	FUV CaF2	2385, 2265	1930, 1990	FUV Silica	2400, 2255	1955, 1985
	NUV B15	2305, 2415	1950, 1980	NUV N2	2285, 2405	1895, 1965
4	FUV CaF2	2410, 2315	1985, 2005	FUV Silica	2395, 2300	1935, 2000
	NUV B15	2295, 2455	1915, 1970	NUV N2	2335, 2460	1955, 1980
5	FUV CaF2	2405, 2245	1975, 1990	FUV Silica	2450, 2250	1960, 2015
	NUV B15	2340, 2400	1945, 1990	NUV N2	2265, 2380	1930, 1970
6	FUV CaF2	2355, 2220	1945, 1960	FUV Silica	2355, 2200	1935, 1960
	NUV B15	2320, 2390	1950, 1955	NUV N2	2310, 2395	1925, 1975
7	FUV CaF2	2420, 2340	1900, 1930	FUV Silica	2360, 2380	1955, 1985
	NUV B15	2305, 2545	1955, 1960	NUV N2	2345, 2470	1915, 1920
9	FUV CaF2	2435, 2410	1970, 1975	FUV BaF2	2445, 2415	1975, 1995
10	FUV CaF2	2485, 2280	1980, 2000	FUV Silica	2495, 2265	1970, 1960
	NUV B15	2370, 2360	1945, 1910			
11	FUV CaF2	2415, 2220	1915, 1945	FUV Silica	2415, 2220	1940, 1970
	NUV B15	2365, 2385	1950, 1930	NUV N2	2375, 2355	1945, 1920
12	FUV CaF2	2400, 2390	1965, 1980	FUV Silica	2415, 2390	1965, 1980
13	FUV CaF2	2500, 2270	2000, 1995	FUV Silica	2510, 2265	1975, 1960
	NUV B15	2390, 2395	1965, 1955	NUV N2	2385, 2345	1960, 1955
14	FUV CaF2	2415, 2445	1965, 2005	FUV Sapphire	2405, 2430	1975, 1995
15	FUV CaF2	2400, 2390	1960, 2010	FUV Sapphire	2395, 2330	1940, 1935
16	FUV CaF2	2345, 2355	1960, 1945	FUV Sapphire	2375, 2365	1965, 1990
17	FUV CaF2	2495, 2335	1985, 2010	FUV Sapphire	2460, 2330	1935, 1990
18	FUV CaF2	2360, 2395	1985, 1990	FUV Sapphire	2390, 2415	1945, 1980
19	FUV CaF2	2440, 2340	1960, 1970	FUV Sapphire	2500, 2355	1955, 1985

Note.

^a HW are the X and Y half-widths in pixels of the elliptical ROI used for source extraction.

$\sigma = 1.5$ pixels ($0''.63$) optimized the source extraction yet did not significantly degrade the spatial resolution of the images. The exception is at closest to the edge of the image (outer $\sim 1'$), where the noise rises rapidly because of the effective exposure time of the image going to small values. To overcome the rising noise level at the edge of the images, we eliminated this outer $\sim 1'$ ring prior to source extraction. The size of the ring was optimized for each of the 52 images by carrying out the source extraction with the optimized source-finding parameters, then visually inspecting the source catalog compared to the image, and finally choosing the region to exclude to eliminate the false source problem.

For clarity, we reiterate the entire source extraction procedure as follows. The image was convolved with a Gaussian with $\sigma = 1.5$ pixels. Local single pixel maxima with a minimum 3σ excess above the local background in a 7×7 sliding box were identified. The resulting candidates were kept in a list if the total excess in the box was more than 8σ above local background. Because of the drift in pointing of the satellite, which was different for each image, each image had decreasing exposure near a different field edge for each image. To exclude the small ring of false sources at the field edge (see above paragraph), we selected an elliptical region of interest (ROI) for each image in CCDLAB. Only the candidates detected within the ROI were fit by elliptical Gaussians and included in the source catalog. The positions and sizes of the ROI were carefully adjusted so that there were no visible false detections up to the outer edge of the ROI. Table 3 gives the ROI for each image (each field and filter combination). Each of the detected sources was fitted using a

constrained parameter (see above) elliptical Gaussian. The counts from each source were corrected to the expected counts from the COG analysis using the constant factor of 1.818 found previously, and the count rate was calculated using the known exposure time.

AB magnitudes of each source were calculated from count rate using the best-fit parameters and the Unit Conversion factors calibrated for the UVIT filters. We used the updated Unit Conversion factors from the most recent calibration of the UVIT detectors reported in Tandon et al. (2020). The errors of the magnitudes were calculated through standard error propagation, where the counts were assumed to follow Poisson statistics. Vega magnitudes were calculated based on the AB-to-Vega magnitude conversion factor for each filter.

Due to the partial overlapping of fields, some sources were detected in the overlap region of two or three adjacent fields. Therefore, we examined every overlap region where adjacent fields overlapped (see Figure 2) to find and combine duplicate detections. For each of the overlap regions, we examined the distribution of separations between sources detected in different fields, up to $5''$. The separation distributions for the overlap of F1 with F2, F1 with F6, and F1 with F7 are shown in Figure 6. The distribution of the number of sources versus separations is determined by the position uncertainties and shows the maximum position offset between each pair of overlapping fields. For example, for F1–F2, F1–F6, and F1–F7 overlaps, the maximum position offset is $\simeq 0''.8$. Considering all overlap regions and the different filters (NUV N2, NUV B15, FUV Silica, FUV Sapphire, and FUV CaF2), the maximum position

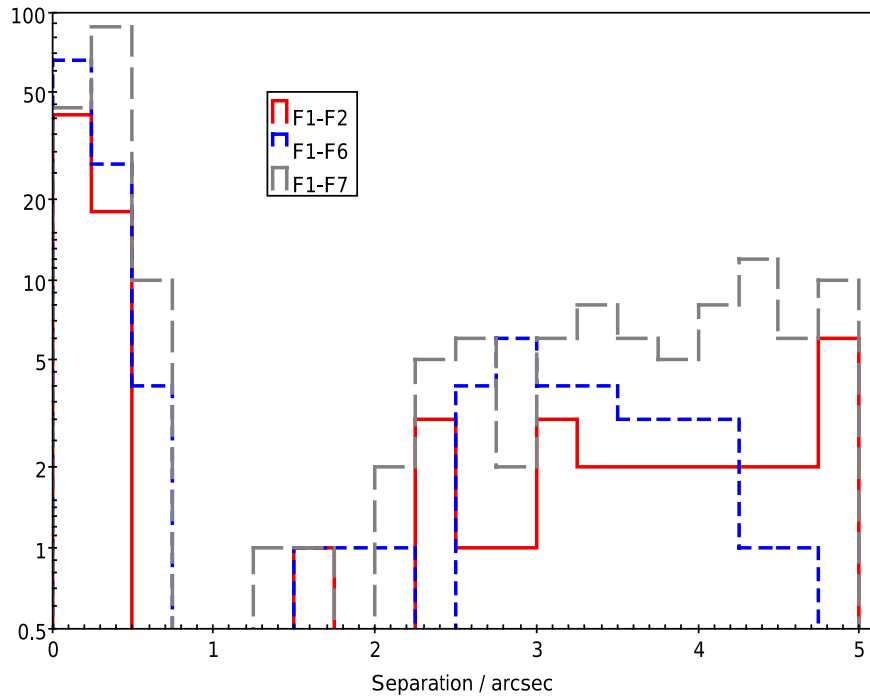


Figure 6. Distribution of separations between NUV N2 sources detected in the overlap region of adjacent fields. The distributions are shown for sources in the Field 1–Field 2 (F1–F2), F1–F6, and F1–F7 overlap regions. For each source from F1 we plot the separations to all sources in the adjacent field up to a maximum of 5". The separations greater than 1" are all consistent with random matches of different sources; the separations less than 1" are consistent with two detections of the same source.

Table 4
Summary of M31 UVIT Source Numbers

Filter	No.		Filter	No.	
FUV CaF2	31337		FUV BaF2	1946	
FUV Sapphire	10923		FUV Silica	6708	
NUV B15	15428		NUV N2	8565	
Filter Pair	No.	Match Radius	Filter Pair	No.	Match Radius
FUV CaF2/FUV BaF2	1659	1''4	FUV CaF2/FUV Sapphire	6943	1''5
FUV CaF2/FUV Silica	6153	1''8	FUV CaF2/NUV B15	11002	1''8
FUV CaF2/NUV N2	5444	1''8	NUV N2/NUV B15	6661	1''8
NUV N2/FUV Silica	3870	1''8	NUV B15/FUV Silica	5689	1''5

offsets were $<1''.5$. A few exceptions with larger position offsets were found for some field/filter combinations: for F3 compared with its adjacent fields for the CaF2 filter, a maximum offset of $2''.2$ was found; for F1 compared with its adjacent fields for the NUV B15 filter, a maximum offset of $1''.8$ was found. The position offsets are expected to be somewhat variable, given that the satellite pointing drift and the drift corrections are different for each field/filter combination.³

We combined the multiple measurements of sources detected in the overlap regions within the maximum position offset of each other. The flux-weighted averages of the R.A., decl., magnitudes, and the errors were calculated. In the final catalog, the combined detections and single detections were included,

and a separate column was created to indicate the field(s) in which the sources were detected.

3. Results and Summary

3.1. Catalog Summary

In Table 4, we list the numbers of sources detected in each of the filters for all of the M31 observations. The CaF2 filter (18 fields) covers the largest area of M31 and has the largest number of sources ($\simeq 31,000$). This filter has the largest bandwidth ($\simeq 125\text{--}175\text{ nm}$). The filters NUV N2 (9 fields), NUV B15 (10 fields), and Silica (10 fields) each cover roughly half of M31 and have $\simeq 8600$, $\simeq 15,000$, and $\simeq 6700$ sources, respectively. The larger number in NUV B15 is expected because of the wider filter bandwidth ($\simeq 210\text{--}235\text{ nm}$) and thus higher sensitivity compared to NUV N2 ($\simeq 275\text{--}285\text{ nm}$) and Silica ($\simeq 165\text{--}175\text{ nm}$) filters. The FUV Sapphire filter (6 fields) has $\simeq 11,000$ sources, which is not surprising because its bandwidth is large ($\simeq 145\text{--}175\text{ nm}$) although less than the FUV

³ Imperfections in the detector distortion correction are the most probable cause of residual distortions at the field edges at the level of $\sim 1''$. These could be further corrected given enough bright sources at the field edges in the short orbit-wise images. The M31 data set is one of a few UVIT data sets that could be used for this.

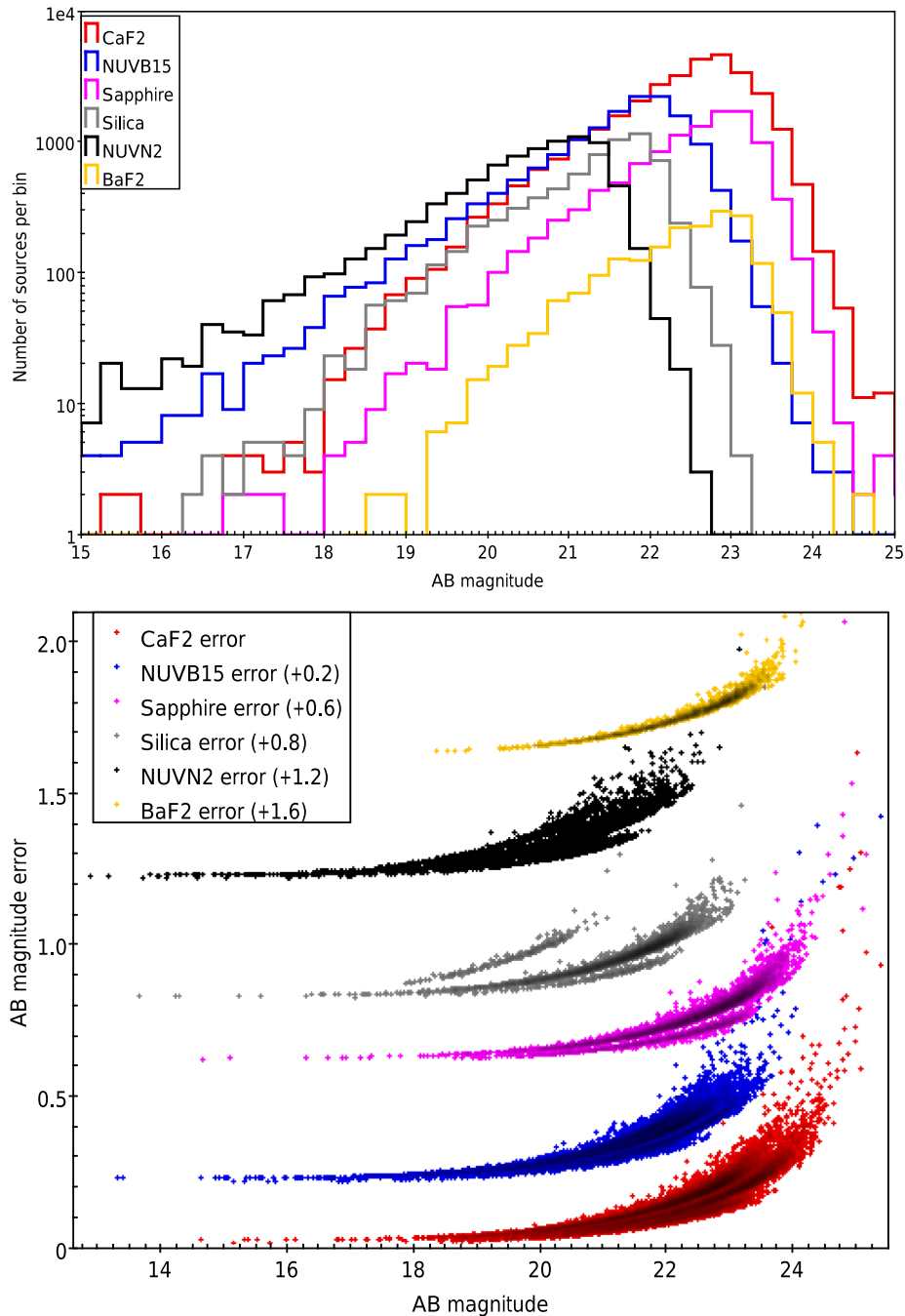


Figure 7. Top: distribution of AB magnitudes for each of the FUV CaF2, NUV B15, FUV Sapphire, FUV Silica, NUV N2, and BaF2 catalogs. Bottom: magnitude errors vs. AB magnitude for the different filters. Observations with significantly different exposure times show up as distinct bands in the error vs. magnitude plot for the different filters.

CaF2 filter. The FUV BaF2 filter covers only one field and so has fewer (≈ 2000) sources.

The distributions of the magnitudes of sources detected in the six different filters are shown in Figure 7. All bright sources in M31, well above the point-source sensitivity limit, are detected, but sources near the sensitivity limit are detected only if they are in uncrowded regions. The exposure times for the different filters ranged from ~ 2000 to $15,000$ s with a mean of ~ 7000 s. The effective areas of the detector/filter combinations range from 7 to 20 cm^2 , and the bandpasses range from 50 to 10 nm (Tandon et al. 2017b). Thus, even for a flat spectrum source, the detected number of photons is expected to vary by up to a factor of 7 (from

exposure time) times 3 (from area) times 5 (from bandpass), or a factor of 100. Thus, sensitivity, in terms of S/N and ignoring effects such as source crowding, is expected to vary a factor of $\sim \sqrt{100} = 10$. The measured magnitude distributions in Figure 7 increase as expected to fainter magnitudes (to $\sim 22\text{--}23$) because of an increasing number of sources at fainter magnitudes. They then decrease beyond that, reflecting the (variable) sensitivity limits of the observations. The sensitivity limit of each image (field/filter combination) is different, but we can estimate approximately the completeness limit of the survey by using the peak in the magnitude distributions. For FUV CaF2, FUV BaF2, and FUV Sapphire, this is at $m_{AB} \simeq 23$; for FUV Silica and NUV B15, this

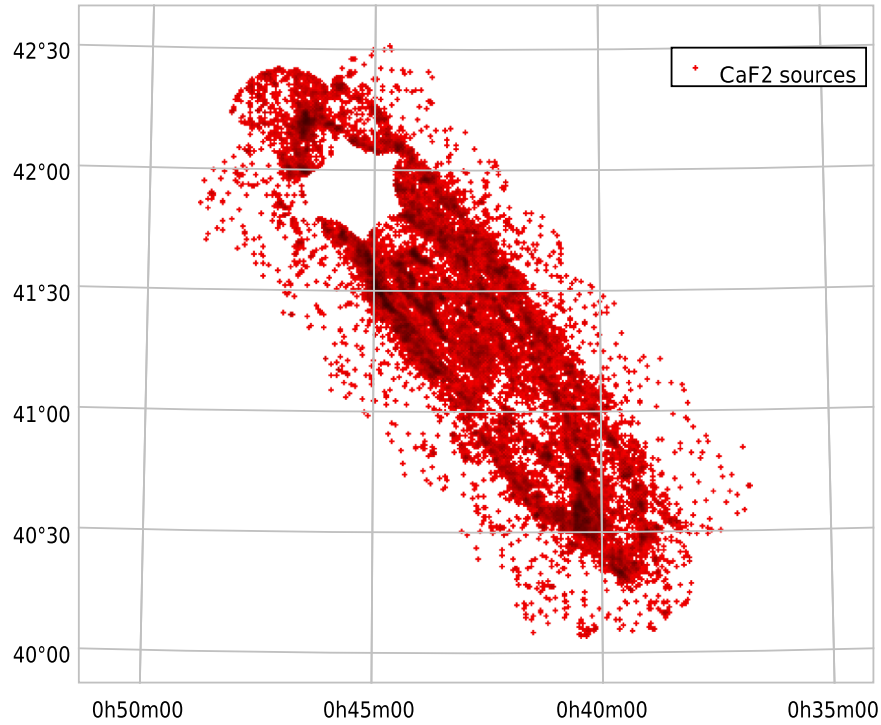


Figure 8. Map of UVIT FUV CaF2 sources (red plus signs) from the M31 survey. Source finding was carried out using a minimum S/N of 8 for the integrated counts in a Gaussian fit to the source. The Gaussian was constrained to have FWHM consistent with the PSF.

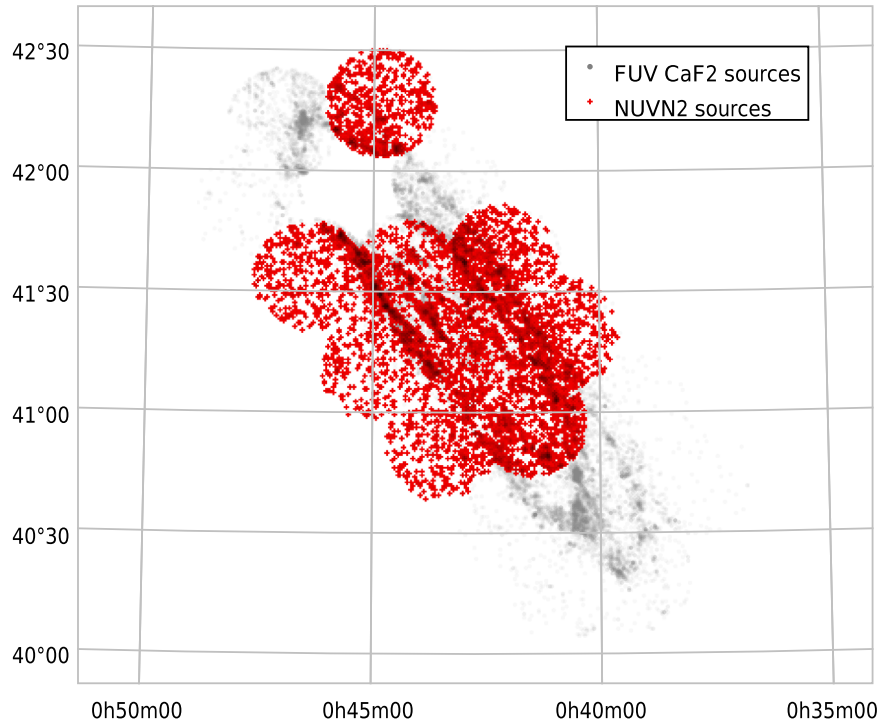


Figure 9. Map of UVIT NUV N2 sources (red plus signs). The CaF2 source map is shown in gray scale in the background.

is at $m_{AB} \simeq 22$; and for NUV N2, this is at $m_{AB} \simeq 21$. The magnitude error versus magnitude plots in the bottom panel of Figure 7 confirm this and illustrate outlying field/filter combinations. For example, for the Silica filter the magnitude errors show a separate band with higher errors for field F2 with the low exposure of 1923 s.

We show the positions of all CaF2 sources in Figure 8. The spiral arms of M31 clearly stand out as regions of high source density. Outside the main body of M31 the source density is nearly constant, which is characteristic of that expected for foreground sources (Milky Way stars) or background extragalactic sources.

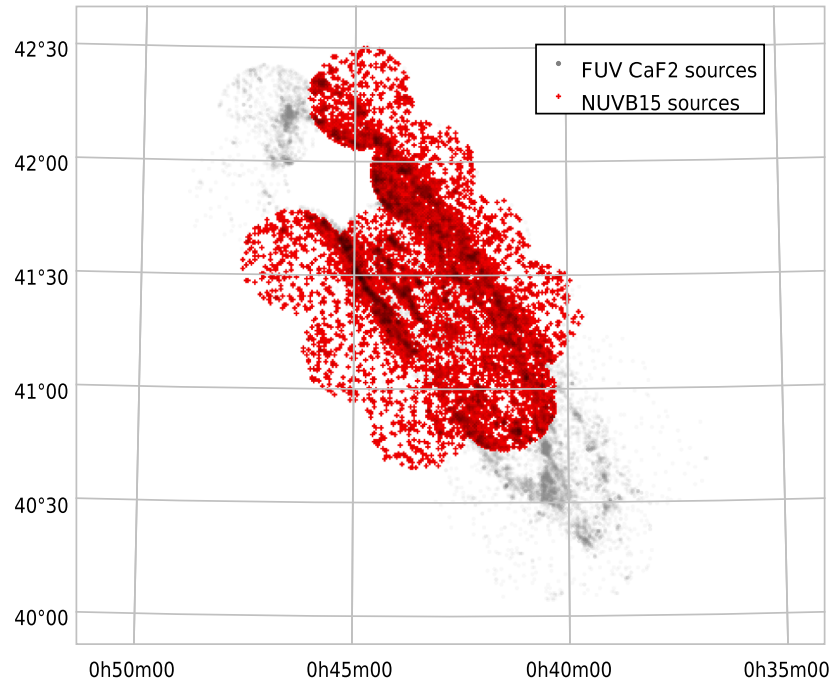


Figure 10. Map of UVIT NUV B15 sources (red plus signs). The CaF2 source map is shown in gray scale in the background.

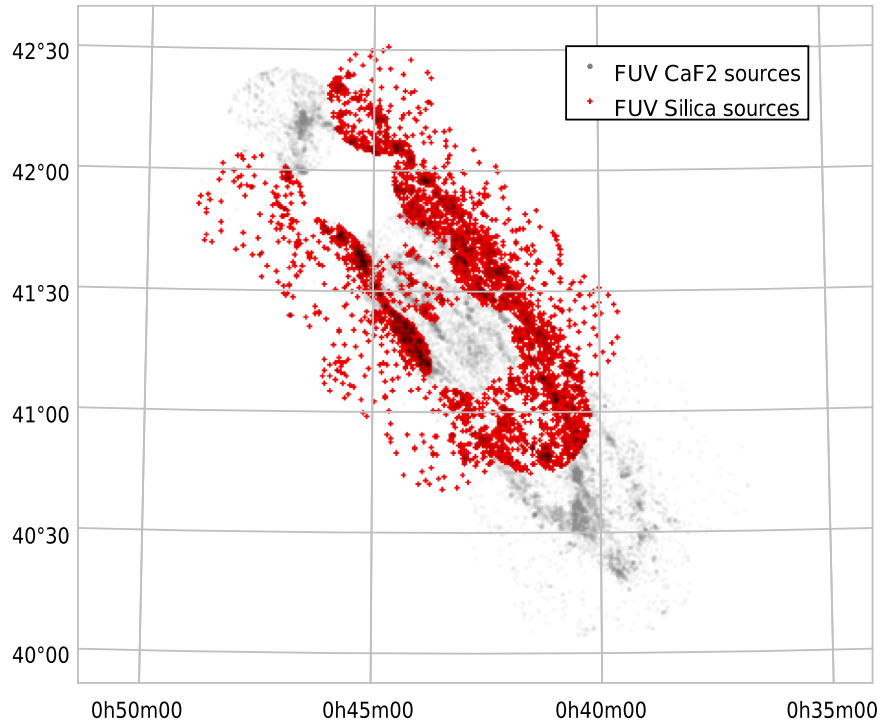


Figure 11. Map of UVIT FUV Silica sources (red plus signs). The CaF2 source map is shown in gray scale in the background.

The NUV N2 sources are shown in Figure 9, overlaid on a grayscale representation of the CaF2 sources. The NUV B15 sources are shown in Figure 10. The areas not observed in NUV N2 and NUV B15 filters were a result of the failure of the NUV channel of UVIT partway through the M31 UVIT survey. The density of foreground sources for NUV N2 is higher compared to CaF2, whereas the density of foreground sources for NUV B15 is intermediate between that for CaF2 and NUV N2. This is because the majority of foreground sources are

expected to be Galactic stars at high Galactic latitude ($-21^\circ.5$) and thus mostly older halo and thick-disk stars, which are relatively faint at FUV wavelengths.

The FUV Silica sources are shown in Figure 11, overlaid on a grayscale representation of the CaF2 sources. The FUV Sapphire sources are shown in Figure 12, and the FUV BaF2 sources are shown in Figure 13. The density of foreground sources for these three FUV filters is comparable to that for CaF2. This is consistent with the foreground sources being

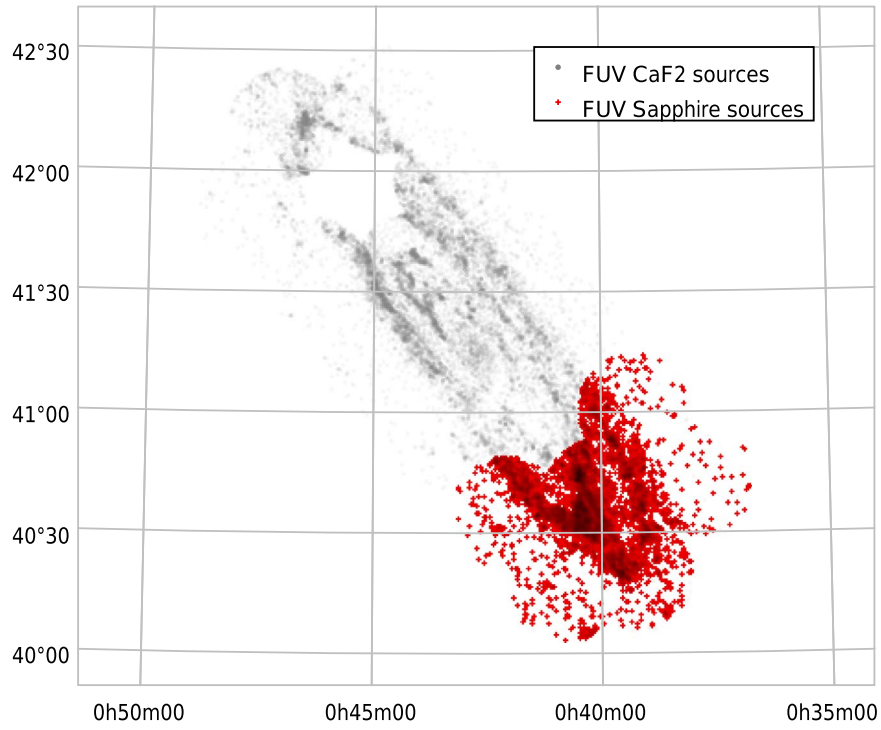


Figure 12. Map of UVIT FUV Sapphire sources (red plus signs). The CaF2 source map is shown in gray scale in the background.

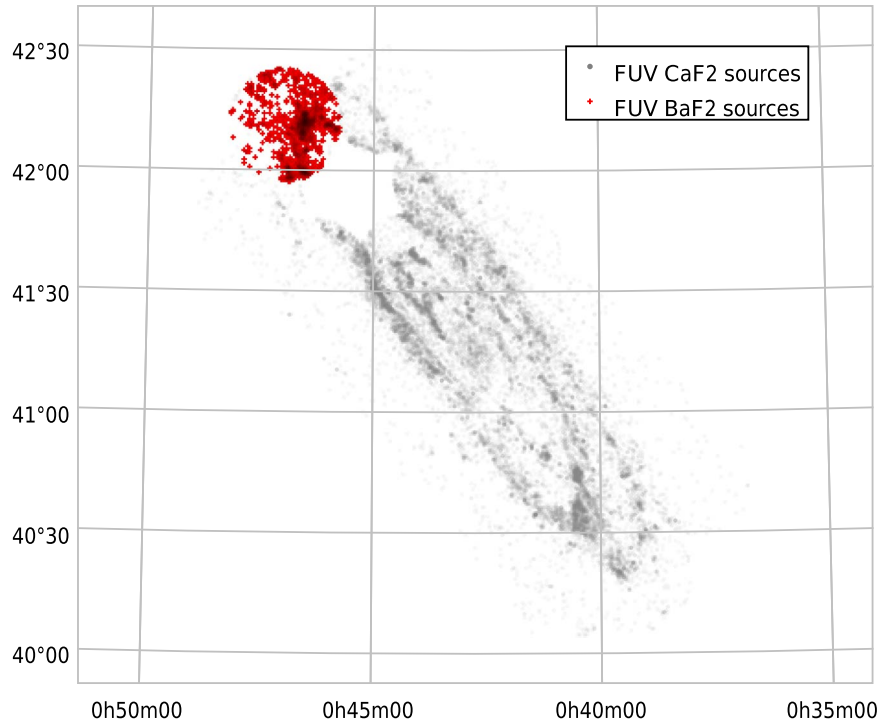


Figure 13. Map of UVIT FUV BaF2 sources (red plus signs). The CaF2 source map is shown in gray scale in the background.

dominated by cooler stars. In all six filters, the spiral arms of M31 are prominent.

3.1.1. Catalog Position Errors: Further Analysis

Above we discussed the position calibration and position error analysis using the *Gaia* catalog positions and the position offsets of UVIT sources detected in the overlap regions. The UVIT

position errors on average over a whole UVIT 28' diameter field are $\sim 0''.2$ – $0''.5$, as summarized in Table 2. The position errors are the smallest ($0''.2$) for the nine fields for which we had NUV N2 filter observations to calibrate with the *Gaia* positions, and worse ($0''.3$ – $0''.7$) for the other nine fields for which we only had NUV B15 or CaF2 filter observations for calibration.

The UVIT position offsets in the overlap regions reveal the position errors in the outer parts of the UVIT fields, typically

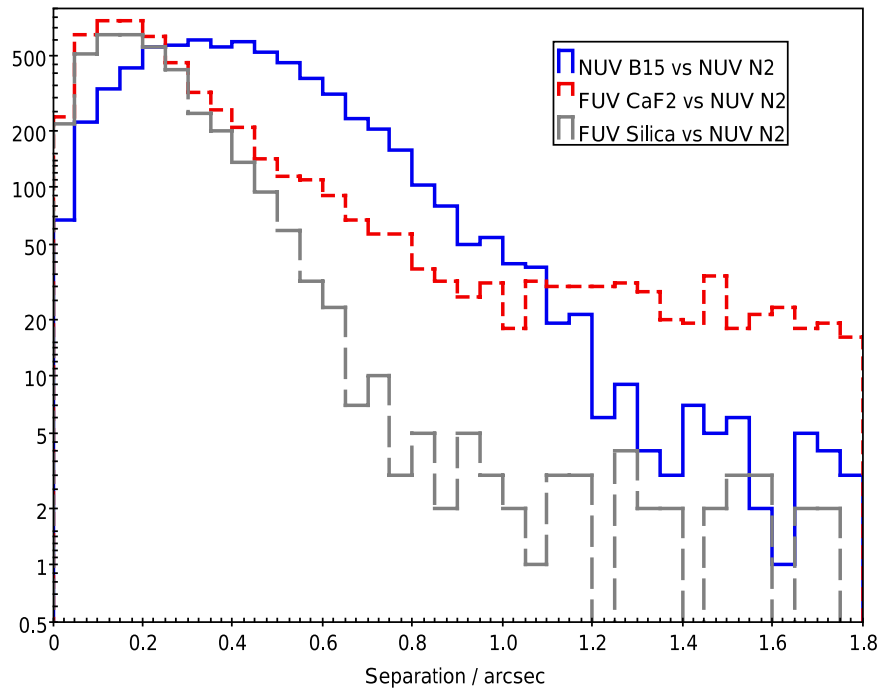


Figure 14. Distribution of NUV B15, FUV CaF2, and FUV Silica position offsets with respect to NUV N2 positions. All sources detected in M31 were used here. This shows that the position accuracy for FUV Silica is best, with a mean offset from NUV N2 of $\approx 0''.15$; NUV B15 positions have the largest offset from NUV N2 positions, with a mean of $\approx 0''.4$; and FUV CaF2 has most sources close to NUV N2 positions, with an offset of $\approx 0''.15$ but with a significant tail of offsets between $\approx 0''.6$ and $\approx 2''$. The tail of the CaF2 offset distribution ($>0''.6$) contains $\sim 8\%$ of the sources measured in both CaF2 and NUV N2 filters.

$\sim 10'$ – $14'$ from the field center. These errors are larger than for the regions closer to the center ($\lesssim 10'$; see Figure 5) and are typically in the range of $\sim 1''$ (see Figure 6).

We carry out here a third position error analysis by comparing positions derived by source fitting the same source in different filters. For this analysis we use the entire UVIT catalog of sources for M31 created here, so it is expected to show a combination of the smaller errors for field centers and larger errors for the field edges. All of M31 was observed in the CaF2 filter (18 fields), and a large part was observed in NUV N2 (9 fields), NUV B15 (10 fields), and FUV Silica (10 fields) filters.

The NUV N2 position errors were determined to be the smallest, as discussed above, so we compare the NUV B15, CaF2, and FUV Silica positions with NUV N2 positions to assess the position errors. Figure 14 shows the separation distributions between the NUV B15 and NUV N2 sources, between the CaF2 and NUV N2 sources, and between the FUV Silica and NUV N2 sources. The FUV Silica positions match NUV N2 positions the best. There were 3870 sources in common for FUV Silica and NUV N2 (Table 4). The mean offset is $\sim 0''.3$, the majority ($>90\%$) of offsets are less than $\sim 0''.5$, and a few sources have position offsets up to $1''.8$. There were 6661 sources in common for NUV B15 and NUV N2. The mean offset is $\sim 0''.5$, the majority ($>90\%$) of offsets are less than $\sim 0''.8$, and a few sources have position offsets up to $1''.8$. There were 5444 sources in common for CaF2 and NUV N2. The mean offset is $\sim 0''.3$, the majority ($>90\%$) of offsets are less than $\sim 0''.8$, and there is an extended tail of position offsets out to $1''.8$.

Because the CaF2 catalog has the largest number of sources, we also compare the NUV N2, NUV B15, FUV Silica, and FUV Sapphire positions with the CaF2 positions. For this analysis we include all matches to the CaF2 sources, rather than

just the closest match, in order to show the effect of accidental matches of unrelated sources. In this way we can verify the separation between real and accidental matches. Figure 15 shows the results. The minima in the distributions indicate the separation between real matches (i.e., the same source detected in different filters) and accidental matches (different sources in the different filters). For CaF2 versus NUV N2 and CaF2 versus NUV B15 the minima are near $\approx 1''.8$. For CaF2 versus Silica the minimum is at $\approx 2''$, and for CaF2 versus Sapphire the minimum is at $\approx 1''.5$. Thus, the maximum position offsets between the different filters is consistent with $1''.5$ – $2''$.

The expected linear relations for accidental matches are plotted as the dashed lines in Figure 15. The linear relations were based on fits to the separation distribution for separations $>3''$ where there are no real matches. These relations can be extrapolated to small separations to estimate the contamination by accidental matches at small separations. It is seen that in the range $1''.5$ – $2''.5$, the number of matches falls below the expected number by a factor of ~ 2 . This is an artifact of the source detection algorithm that detects sources in a 7 by 7 pixel box ($2''.9$ by $2''.9$) and fits detected sources by an elliptical Gaussian. This has the effect that real sources closer together than $2''.9$ are often not fit as two separate sources or not fit at all, consistent with the factor of ~ 2 deficit of accidental matches for separations in the range of $1''.5$ – $2''.5$. Thus, we conclude that we are missing some fraction ($\sim 50\%$) of closely separated pairs, instead missing them or fitting them as single sources. This limited ability to separate closely separated pairs is a common limitation for source separations close to or less than the detector resolution. Currently the source-fitting code fits a single PSF within a search box. We are developing a code that fits multiple PSFs within a search box with the aim to improve results for closely separated sources.

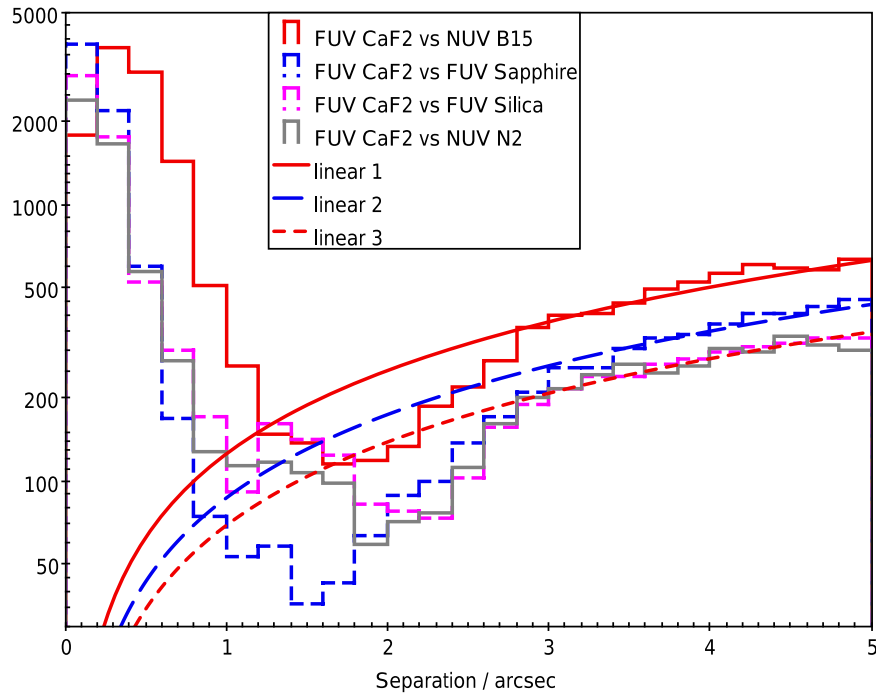


Figure 15. Offsets for all sources in each of the NUV B15, FUV Sapphire, FUV Silica, and NUV N2 catalogs from FUV CaF2 source positions. All sources are included (not just the nearest source) to illustrate the effect of accidental matches. The accidental matches follow a trend that is linear in separation and is shown by the dashed lines, with different normalizations for the different matches. There are deficits below the linear trends for separations between $\approx 1''.4$ and $2''.5$. These deficits shows that the source finding is missing a significant fraction (\sim half) of closely separated sources in this range of separations.

3.2. Sample Color–Magnitude Diagram

As an example of the utility of the catalog and photometry for study of stars in M31, we construct a color–magnitude diagram (CMD) from one of the fields, F4, with a small number of stars. Field F4 has 1061 sources with both CaF2 and NUV B15 magnitudes. The locations of the point sources from the catalog are shown in the top left panel of Figure 16. F4 is located west of the bulge at the edge of M31 (Figure 2); thus, the easternmost part of F4 (marked in red in Figure 16) should be dominated by sources in M31, and the western part of F4 (marked in blue) should be dominated by foreground stars.

The CMD, with CaF2 AB magnitude and color (CaF2 m_{AB} –NUV B15 m_{AB}), is shown in the top right panel of Figure 16. We provide only a preliminary interpretation here and leave a detailed analysis for future work. The computed CMD diagram, using Castelli and Kurucz stellar model atmospheres (Castelli & Kurucz 2004) and the UVIT filter profiles, is shown in the bottom panel of Figure 16. We use their recommended T_{eff} and radii for stars of spectral types O3V, O5V, O8V, B0V, B3V, B5V, B8V, A0V, A5V, F0V, and several later spectral types. However, spectral types later than F2V have UV colors off the diagram (more negative) and so are not considered further. First, we consider main-sequence stars at the distance of M31 ($d_{\text{M31}} = 780$ kpc), plotted as filled symbols in Figure 16. Evolved blue giants are mimicked here by increasing the radius by a factor of 4–40, for purpose of illustration. The effect of increasing extinction A_V from 0.2 to 1.2, with 0.2 the value of foreground extinction to M31, is shown by the dotted lines for two cases: a B3V star and an A5V star. Extinction increases the position nearly vertically downward.

Now we compare to the observed CMD in the top right panel of Figure 16. The synthetic CMD shows that the left side of the CMD can be populated with synthetic stars of spectral type O3 to A0 with extinction between 0.2 and 1.2, and it is further filled if

there is some mixture of evolved blue stars with larger radii. Thus, the vast majority of the red points (the SE set) and $\sim 1/2$ of the blue points are consistent with a location in M31 and being normal (main-sequence or evolved) blue stars (earlier than A0). Next, we compare the synthetic CMD for foreground stars with the left side of the observed CMD. In the bottom panel of Figure 16, example foreground stars with distances 0.78, 2.5, and 7.8 kpc are plotted as open symbols. Hot stars would be too luminous to be consistent with the observed points; thus, there are no hot (earlier than A0) stars in the field. But cooler foreground stars of spectral types A5–F2 at distances of ~ 0.8 –8 kpc are consistent with the observed points. In fact, the observed points with NUV B15–CaF2 color < -2.4 are only consistent with being foreground sources. The fact that some M31 objects (right group in top right panel of Figure 16) are spatially in the NW set and some foreground objects (left group in top right panel) are in the SE set is expected: the foreground objects should be uniformly distributed across the field, and M31 objects do not have a sharp edge with increasing distance from the center of M31.

3.3. Summary and Catalog Release

The M31 UVIT catalog consists of six main tables, one for each filter (FUV CaF2, FUV BaF2, FUV Sapphire, FUV Silica, NUV B15, and NUV N2), and eight filter-matched tables, one for each filter pair listed in Table 4. Table 4 also gives the maximum radius for matching sources between filters, determined using separation distributions described above and illustrated in Figure 15. A sample of five entries from the FUV CaF2 catalog is given in Table 5. The matched-filter tables give the same six columns as listed in Table 5 for each of the two filters, labeled by filter (total 12 columns), plus a 13th column that is the separation between the best-fit coordinates from the two filters. A sample of the pair-matched catalog is given in Table 6.

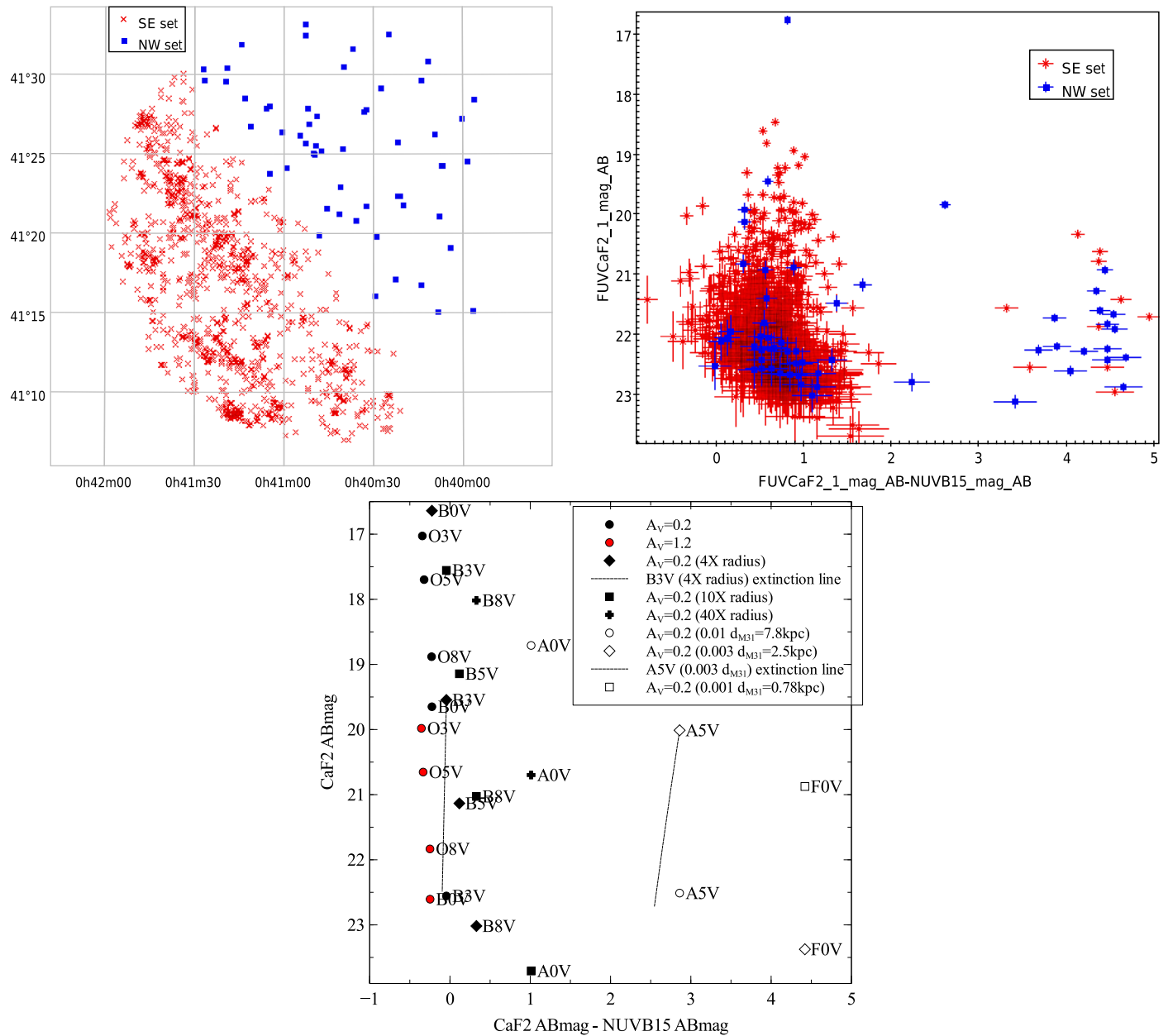


Figure 16. Top left: sources with CaF2 and NUV B15 magnitudes in field F4 separated spatially into two groups: the NW set expected to be mostly foreground objects and the SE set of mostly M31 objects. Top right: CMD for SE and NW sources. Bottom: computed CMD diagram for stars at the distance of M31 ($d_{M31} = 780$ kpc) with indicated spectral type and extinction (solid symbols). Blue giants/supergiants are mimicked by increasing the radius. The effect of increasing extinction A_V from 0.2 to 1.2 is shown for a B3V and an A5V star. Sample foreground stars of indicated distances are plotted as open symbols.

Table 5
AstroSat UVIT M31 Point-source Catalog

FUV CaF2 R.A. (° J2000)	FUV CaF2 Decl. (° J2000)	FUV CaF2 (AB mag)	FUV CaF2 (Vega mag)	FUV CaF2 (mag err)	Field No.
10.0142	40.4323	22.038	19.637	0.087	14, 15, 19
10.0115	40.4359	22.219	19.818	0.095	14, 15, 19
10.0375	40.4643	22.633	20.232	0.124	14, 15, 19
10.0468	40.4601	21.869	19.468	0.081	14, 15, 19
10.0051	40.4407	22.738	20.337	0.122	14, 15, 19

(This table is available in its entirety in machine-readable form.)

Table 6
The *AstroSat* UVIT M31 Filter-matched Catalog

FUV CaF2						FUV BaF2						Sep. (")
R.A. (° J2000)	Decl. (° J2000)	AB (mag)	Vega (mag)	Error (mag)	Field	R.A. (° J2000)	Decl. (° J2000)	AB (mag)	Vega (mag)	Error (mag)	Field	
11.4490	42.2231	22.980	20.579	0.149	9, 11	11.4488	42.2232	22.983	20.777	0.206	9	0.42
11.5001	42.2948	22.632	20.231	0.124	9, 11	11.5000	42.2947	22.989	20.783	0.212	9	0.30
11.4743	42.2399	22.259	19.858	0.107	9, 11	11.4741	42.2400	23.298	21.092	0.258	9	0.44
11.4932	42.3005	22.299	19.898	0.106	9, 11	11.4932	42.3005	22.675	20.469	0.184	9	0.22
11.4773	42.2210	21.857	19.456	0.086	9, 11	11.4773	42.2210	22.056	19.850	0.136	9	0.09

(This table is available in its entirety in machine-readable form.)

In this study, we have analyzed the data from the M31 UVIT survey to produce a point-source catalog with nearly 75,000 sources detected in FUV or NUV wavelengths. This catalog will be used in future for studies of stars and other sources in M31 that have been measured at optical and other wave bands, such as infrared and X-ray.

This project is undertaken with the financial support of the Canadian Space Agency and from the Natural Sciences and Engineering Research Council of Canada. We thank the referee for recommendations that led to improvements in the paper.

ORCID iDs

D. A. Leahy  <https://orcid.org/0000-0002-4814-958X>

References

- Bianchi, L., Efremova, B., Hodge, P., & Kang, Y. 2012, *AJ*, **144**, 142
- Bianchi, L., Kang, Y., Hodge, P., Dalcanton, J., & Williams, B. 2014, *AdSpR*, **53**, 928
- Calabretta, M. R., & Greisen, E. W. 2002, *A&A*, **395**, 1077
- Castelli, F., & Kurucz, R. L. 2004, arXiv:astro-ph/0405087
- Davidge, T. J. 1993, *ApJ*, **409**, 190
- Gil de Paz, A., Boissier, S., Madore, B. F., et al. 2007, *ApJS*, **173**, 185
- Ibata, R., Irwin, M., Lewis, G., Ferguson, A. M. N., & Tanvir, N. 2001, *Natur*, **412**, 49
- Kang, Y., Bianchi, L., & Rey, S.-C. 2009, *ApJ*, **703**, 614
- Kang, Y., Rey, S.-C., Bianchi, L., et al. 2012, *ApJS*, **199**, 37
- Massey, P., Armandroff, T. E., & Conti, P. S. 1986, *AJ*, **92**, 1303
- Massey, P., Olsen, K. A. G., Hodge, P. W., et al. 2006, *AJ*, **131**, 2478
- McConnachie, A. W., Irwin, M. J., Ferguson, A. M. N., et al. 2005, *MNRAS*, **356**, 979
- Morrissey, P., Conrow, T., Barlow, T. A., et al. 2007, *ApJS*, **173**, 682
- Postma, J., Hutchings, J. B., & Leahy, D. 2011, *PASP*, **123**, 833
- Postma, J. E., & Leahy, D. 2017, *PASP*, **129**, 115002
- Singh, K. P., Tandon, S. N., Agrawal, P. C., et al. 2014, *Proc. SPIE*, **9144**, 91441S
- Subramaniam, A., Tandon, S. N., Hutchings, J., et al. 2016, *Proc. SPIE*, **9905**, 99051F
- Tandon, S. N., Hutchings, J. B., Ghosh, S. K., et al. 2017a, *JApA*, **38**, 28
- Tandon, S. N., Postma, J., Joseph, P., et al. 2020, *AJ*, in press (arXiv:2002.01159)
- Tandon, S. N., Subramaniam, A., Girish, V., et al. 2017b, *AJ*, **154**, 128
- Thilker, D. A., Hoopes, C. G., Bianchi, L., et al. 2005, *ApJL*, **619**, L67
- Williams, B. F., Lang, D., Dalcanton, J. J., et al. 2014, *ApJS*, **215**, 9